Three-dimensional Structure of a Single Filament in the *Limulus* Acrosomal Bundle: Scruin Binds to Homologous Helix-Loop-Beta Motifs in Actin

Michael F. Schmid, Jacob M. Agris, Joanita Jakana, Paul Matsudaira,* and Wah Chiu

Verna and Marrs McLean Department of Biochemistry and The W. M. Keck Center for Computational Biology, Baylor College of Medicine, Houston, Texas 77030; and *Whitehead Institute for Biomedical Research and Department of Biology, Massachusetts Institute of Technology, Cambridge, Massachusetts 02142

Abstract. Frozen, hydrated acrosomal bundles from *Limulus* sperm were imaged with a 400 kV electron cryomicroscope. Segments of this long bundle can be studied as a *P1* crystal with a unit cell containing an acrosomal filament with 28 actin and 28 scruin molecules in 13 helical turns. A novel computational procedure was developed to extract single columns of superimposed acrosomal filaments from the distinctive crystallographic view. Helical reconstruction was used to generate a three-dimensional structure of this computationally isolated acrosomal filament. The scruin molecule is organized into two domains which contact two actin subunits in different strands of the same actin filament. A correlation of Holmes' actin filament model to the density in our acrosomal filament map shows that actin subdomains 1, 2, and 3 match the model density closely. However, actin subdomain 4 matches rather poorly, suggesting that interactions with scruin may have altered actin conformation. Scruin makes extensive interactions with helix-loop-beta motifs in subdomain 3 of one actin subunit and in subdomain 1 of a consecutive actin subunit along the genetic filament helix. These two actin subdomains are structurally homologous and are closely spaced along the actin filament. Our model suggests that scruin, which is derived from a tandemly duplicated gene, has evolved to bind structurally homologous but non-identical positions across two consecutive actin subunits.

BIOCHEMICAL studies have identified several families of actin cross-linking proteins which organize actin filaments as bundles in cells (Hartwig and Kwiatkowski, 1991; Matsudaira, 1991). The largest and best characterized family of actin cross-linking proteins consists of fimbrin, α-actinin, spectrin, dystrophin, filamin, and ABP120. They are characterized by a pair of 28-kD actin binding domains. Fimbrin is found in intestinal brush border microvilli and hair cell stereocilia while α-actinin is located within the actin bundle of the stress fiber. A second family of actin cross-linking proteins is defined by fascin, a 56-kD actin binding protein (Kane, 1975) found in actin bundles of sea urchin sperm acrosomal process, egg microvilli, and coelomocyte filopodia. Fascin is homologous with the *singed* gene product of *Drosophila* and vertebrate 55-kD protein (Bryan et al., 1993). Unlike fimbrin, fascin displays no internal homology. Filaments bundled by fascin display a distinctive 120 Å transverse banding pattern. Image analysis suggests that a fascin cross-link is located every four or five actin subunits in a filament (DeRosier et al., 1977). A third family of actin bundling proteins includes villin and dematin (Rana et al., 1993). Both proteins cross-link actin filaments through an 8-kD COOH-terminal headpiece domain. Because proteins within each family have homologous actin binding domains, they are expected to bind to identical sites on actin. The same assumption may not be valid for bundling proteins belonging to different families because their actin binding domains are unrelated in sequence and presumably in folded conformation.

Scruin (102 kD), another actin binding and bundling protein, is found in a 1:1 complex with actin in the acrosomal process of *Limulus* sperm (Schmid et al., 1991). The protein sequence of scruin is unrelated to any known actin binding proteins but reveals, like fimbrin, a tandem pair of homologous domains (Way, M., and P. Matsudaira, manuscript submitted for publication). Sequence comparisons reveal homology within each domain with *kelch*, a gene in *Drosophila* that is important in nutrient transport into the oocyte and in the maintenance of a cellular structure called the ring canal (Xue and Cooley, 1993), and with MIPP, a mouse placental protein of unknown function (Chang-Yeh et al., 1991). Their similarity with scruin suggests a cytoskeletal function and

Address all correspondence to W. Chiu, Verna and Marrs McLean Department of Biochemistry and the W. M. Keck Center for Computational Biology, Baylor College of Medicine, Houston, TX 77030

they may form a new family of actin cross-linking proteins. The actin binding domains in this family of proteins have not been identified.

To understand the structural basis of actin cross-linking and bundling, we have been studying the acrosomal process of *Limulus* sperm by electron cryomicroscopy. Besides its simple biochemical composition, the actin bundle of the *Limulus* acrosomal process is structurally unique because our earlier electron cryo-microscopic studies showed it can be considered as a single three-dimensional crystal in space group *P1*, with 28 actin subunits and scruin molecules per unit cell. The unit cell parameters are $a = b = 147$Å, $c = 762$Å, $\alpha = 90°$, $\beta = 90.6°$, and $\gamma = 120°$ (Schmid et al., 1991). A strong non-crystallographic 2_1 screw symmetry is present due to the helical arrangement of actin and scruin. Using the intermediate voltage electron microscope to reduce the chromatic aberration effects and the computer controlled spot-scan imaging to reduce the beam-induced specimen movement (Brink and Chiu, 1991), we have been able to image the ice-embedded acrosomal bundle to better than 7 Å resolution (Schmid et al., 1993*b*). A high resolution three-dimensional structure would allow us to describe the location of the scruin and actin filaments in the bundle and their interactions.

As a first step in describing the high resolution structure of the acrosomal bundle, we are using helical symmetry to determine the structure of isolated acrosomal filaments from the bundle. A major problem when trying to approach the helical reconstruction of the acrosomal filaments is that images of filaments when projected onto a plane appear to interdigitate or even overlap, much like a zipper, because of their close juxtaposition. A biochemical solution to this problem is to disassemble the bundle into individual filaments (Bullitt et al., 1988). However, this potentially alters the structure of the cross-linking protein since interactions with neighboring filaments are destroyed. We describe here a computational method for isolating a projection image of a column of superimposed acrosomal filaments from the bundle using images taken with a 400 kV cryomicroscope. Using this method we have calculated a three-dimensional map of a single acrosomal filament in the bundle by helical reconstruction techniques. To this structure we have fitted an actin filament based on the F-actin model proposed by Holmes et al. (1990) and have described the interactions between actin and scruin molecules.

Materials and Methods

Acrosomal Bundle Preparation and Electron Cryomicroscopy

Acrosomal bundles were prepared as described previously (Schmid et al., 1991). Flood beam images of frozen, hydrated acrosomal bundles kept at −170°C were recorded with 400 keV electrons at 15,000–30,000 magnification in a JEOL4000 electron microscope interfaced with an external computer control (Brink et al., 1992; Schmid et al., 1993*b*). The criteria for choosing segments of bundle images for subsequent computer processing were based on overall length of bundle, straightness, lack of significant twist of the bundle, lack of fraying of the outside filament, and diffraction quality as shown in optical diffractograms. Moreover, the image segment had to exhibit an apparent characteristic view suggesting the *h0l* orientation of the bundle. The chosen image segments were scanned at 4.67 Å/pixel in a Perkin Elmer microdensitometer (1010M; Perkin-Elmer Corp., Norwalk, CT).

Computational Extraction of an Acrosomal Filament Representing a Column of Superimposed Filaments in the Acrosomal Bundle

The rationale for computationally isolating and averaging a projection of a single column of acrosomal filaments from the acrosomal bundle is as follows. A segment of the bundle is considered to be a bounded crystal of ~80 filaments packed in a pseudohexagonal array. There are three distinct views arranged ~60° apart azimuthally where the acrosomal filaments align coherently into superimposed columns (Schmid et al., 1991). Typically, 10–11 columns of filaments span the width of the bundle in these projections and filaments at the edges of the bundle are easily seen. Among many bundle images being analyzed computationally, we chose images of the acrosomal bundles with the (*h0l*) or its equivalent projection view for the current investigation. Those images were identified initially by visual inspection and then confirmed by the low phase residual of the 2_1 screw symmetry in the computed diffraction pattern of the chosen images (Schmid et al., 1991). Therefore, the chosen bundle segments for the following operation have the filaments parallel to the bundle axis and have negligible twist. Three bundle segments from separate micrographs were used, representing data from ~1,200 unit cells.

Because edge filaments lack outside neighbors, we can use them to define the left and right sides of a column of filaments. With the left and right edge filament columns as models for the right and left neighbors, respectively, a projection image of a superimposed column of filaments can be isolated. Fig. 1 illustrates this procedure for a simplified and hypothetical case of a five-filament-column-wide bundle. The bundle is shifted so that filament column 1 of the right-shifted bundle (Fig. 1 *b*, *right*) is superimposed on filament column 4 of the original image (Fig. 1 *a*). Likewise, filament column 5 of the left-shifted bundle (Fig. 1 *b*, *left*) is shifted to superimpose on filament column 2 of the original image. This requires two independent shifts of the bundle in opposite directions. The spatial shift corresponds to a phase shift in Fourier space and we have carried out this manipulation in Fourier space. Fig. 1 *c* illustrates the result of subtracting Fig. 1 *b* from 1 *a*, and Fig. 1 *d* represents the floated and boxed filament ready for merging.

The magnitude and direction of the optimal image shift in the above scheme is an integral multiple of the unit cell spacing along the crystallographic unit cell vector *a* of the bundle ($a = 147$ Å). This vector can be determined from the reciprocal lattice vector a^* in a computed Fourier transform of a boxed image array such as Fig. 2 *a*. The *a* (or a^*) vector has both horizontal and vertical components in the boxed image array (or in its Fourier transform). Its magnitude and direction can be refined accurately to within 0.01 pixel using the SPECTRA software (Schmid et al., 1993*a*).

The two shifted images must be subtracted from the original image using the appropriate weights so that the signal from each edge filament column (1 or 5) cancels the corresponding filament column 4 or 2 from the original image (Fig. 1 *c*). This will isolate the filament column (filament 3 in our example) that lies between the two shifted edge filament columns. Weights were determined by linear estimation based on average signal strength along a filament's helix axis. This procedure has been carried out iteratively for all the filament columns in the bundle by shifting the bundle so that each filament column lies between the two shifted edge filaments. The eight or nine resulting isolated filament columns from each bundle are merged by vector summation in Fourier space. The result is a single acrosomal filament which is an average of isolated filament columns from each bundle segment. This single acrosomal filament is subjected to subsequent helical reconstruction procedures.

Moore et al. (1970) proposed another method of isolating closely packed filaments. The procedure of this reconstruction is different in a number of ways: (*a*) their method assumed that all filaments in a side-by-side array have equal density and contrast, whereas ours scales for the observed variable numbers of superimposed filaments in our bundle; (*b*) theirs averaged all filaments at once whereas ours takes the sum of only the internal filaments after each of them is separately isolated; and (*c*) theirs was most effective for a small number of filaments where the local maxima are above the noise, whereas ours is appropriate for these bundles which are up to 11 filaments wide.

Helical Reconstruction of Isolated Acrosomal Filaments

Based on our previous results (Schmid et al., 1991) that actin polymerized preferentially at one end of the bundle, one can recognize the polarity of the filaments in the bundle. Layer lines from each isolated acrosomal filament were extracted according to the helical selection rule of 28 subunits

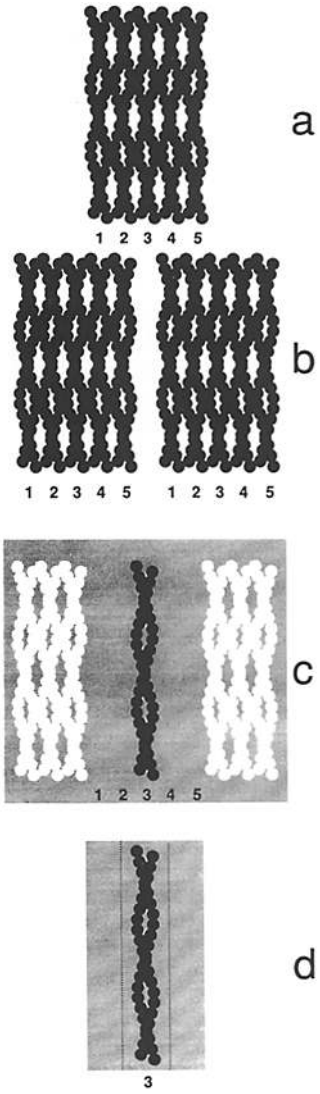

Figure 1. Computational filament isolation. The chosen images have the characteristic (*h0l*) view in which columns of filaments are seen in projection. In this diagram only five columns of filaments in a bundle are shown for simplicity. The numbers label each column in the bundle. The procedure for isolating the image of a column of filaments is as follows: A duplicate image is overlaid over the original image. If the duplicate image were subtracted from the original image, then no bundle would remain because the images overlap completely. However, if the duplicate image is shifted to the right with respect to the original image by one column of filaments, then a subtracted image would retain the image of a single column of filaments corresponding to the left edge of the bundle. This procedure is carried out for each column of filaments in the bundle. For internal filaments, as shown here, duplicate images must be shifted to the right and left of the original image by three unit cells in this case to remove both neighboring filaments. The procedure was repeated for each of the internal columns of filaments.

in 13 turns which was derived from the computed diffraction pattern of images of the bundle (Schmid et al., 1991). The helical unit cell spacing is 762 Å, the same as the c unit cell spacing of the bundle crystal. A total of 21 layer lines out to 58th layer line corresponding to 13.1 Å resolution were extracted. Along the layer lines, data up to 13 Å were included except those having higher order Bessel functions overlap at high resolution (for example, the 22nd order on layer line 6).

Some slight corrections for tilt and origin shift were applied to the phases of the extracted layer lines, although the choice of specimen orientation and the isolation procedure assured that such corrections would be very small. Defocus was determined by computing the Fourier transform of a large area of the micrograph including the bundle. Defocus correction by phase reversal and Wiener filtering was applied to the extracted layer lines for two of the three images whose contrast transfer function (CTF)[1] rings could be seen in the computed diffraction patterns (Schmid et al., 1993*b*). The third image had no detectable CTF rings, so it was assumed to be very close to focus and only the phase correction was made with respect to the other two images.

The CTF corrected layer lines from the three isolated and averaged acrosomal filaments were merged by azimuthal and axial shifting. After this, Fourier-Bessel deconvolution and helical reconstruction from the resulting radial and azimuthal structure factors were carried out to produce a three-dimensional helical reconstruction as established previously (DeRosier and Klug, 1968). All of these operations have been computed with software written in FORTRAN (Jeng et al., 1989; Schmid et al., 1993*a*,*c*) and run under a UNIX operating system on a Silicon Graphics Inc. Indigo. To correct for a Fresnel fringe at the edge of the bundle image, which affects our single filament isolation, a real space weighting function was applied to the final map as described below.

One consequence of our isolation method was that the density in the center of the filament in the reconstruction was too low, for the following reason. The defocus causes a low density Sinc (sin(x)/x) fringe ~50 Å wide on the outer side of the edge filament columns. This negative dip in the density is subtracted by our procedure from the filament column to be isolated. Therefore the perimeter of the isolated filament column has a density higher than it should, while the center is underestimated. The CTF correction of the isolated and extracted layer lines does not take this overweighing into account. The three-dimensional map was corrected with a radial cosine function of wavelength 100 Å with its peak at the center of the helix and an amplitude of 6% of the total contrast. This correction produced a density map for which a single contour level gave the proper volume for both actin and scruin. This empirical observation was the criterion we used for the correction.

Three-dimensional Model Fitting of F-Actin Filament to Our Map

A real-space correlation function in three dimensions between the density in our reconstruction and that derived from the atomic coordinates of Holmes' filament model (Holmes et al., 1990) was calculated to determine their best fit. As a simple approximation, each atom in the Holmes model was assigned the same density value. A search procedure was devised to find the best overlap of their density with ours, with the constraint that their model's helix axis is kept coincident with the helix axis of our map. The search for this overlap was performed by stepwise rotation of 1° and axial translation of 0.5 Å. The optimal fit is the orientation of the Holmes model which yielded the highest correlation peak as shown in Fig. 3. Since our density map contains both actin and scruin, it is possible that the fit would be made to scruin instead of actin. Therefore, radial and density cutoffs were applied to prevent the search for actin from finding the density of the more massive scruin protein. Furthermore, we confirmed quantitatively the polarity of the actin in Holmes model with respect to our map by computing the correlation with both possibilities (up and down).

CHAIN (courtesy of Dr. F. Quiocho) was used initially to visualize the results of the fitting of the model to our density map and identify the portions of the actin structure which were in most intimate contact with the density assumed for the scruin molecule. Holmes' model was turned into a low resolution "map" by centering a decreasing density sphere of 10 Å radius at each C_α, using a program written locally, and then contouring the resulting integrated density map to produce a space-filling model with 100% of the volume of an actin subunit. Each subunit was displayed in a different color in an opaque rendering mode. Our three-dimensional density map was also contoured at 100% volume of the actin–scruin complex. It was rendered semi-transparent in figures where the actin model also appears, to facilitate the visualization of the match of the actin subunits into the actin part of our map and the relationship of the actin to the scruin. The actin model was also used as a mask to carve out the actin part of our reconstruction map after fitting. All the surface renderings of our maps and the low resolution representation of Holmes F-actin filament model were done with the graphics program of EXPLORER from Silicon Graphics Inc. (SGI), with modules written to read MRC data format. The α-carbon trace of the actin x-ray structure was displayed using the Ribbon program (Carson, 1987) run on an SGI workstation.

Sequence Alignment of the Helix-Loop-Beta in Subdomains 1 and 3 of Actin

The two helices of the helix-loop-beta motifs in subdomains 1 and 3 of actin (Kabsch et al., 1990) were displayed graphically with the Ribbon program. First we identified the interior residues and then oriented them facing in the same way. This produced an alignment based on structural homology rather than sequence homology. We were then able to read out the surface residues which are potentially involved in interacting with the scruin.

Results and Discussion

Image of Acrosomal Bundle and Its Computationally Isolated Single Acrosomal Filament

Because of the cylindrical shape of the acrosomal bundle, it

1. *Abbreviation used in this paper*: CTF, contrast transfer function.

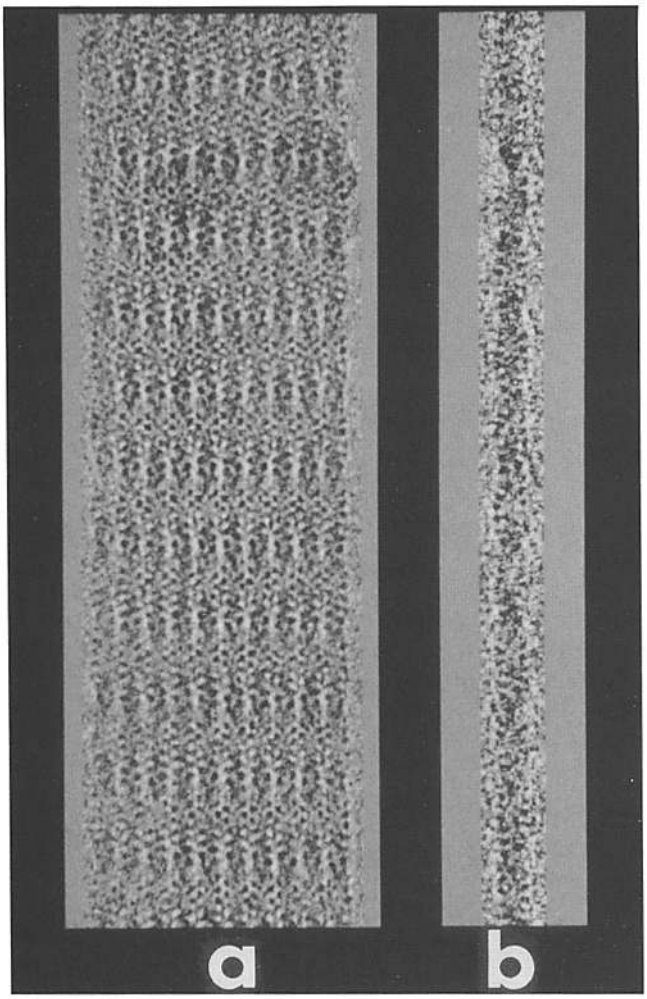

Figure 2. (*a*) 400 kV scanned electron image of an acrosomal bundle embedded in vitreous ice. This bundle is 1,270Å wide. (*b*) One central isolated acrosomal filament obtained from the helix isolation procedure. A helical filament is contained in a rectangular matrix with a width of 2 unit cells and a length of ~5.5 unit cells. The filament pixels were averaged 2 × 2 relative to the original scan size for purposes of display for this figure. Note the low density at the sides of the isolated filament compared with the crystal from which it was computationally derived.

can be oriented randomly in different ice-embedded samples. Fig. 2 *a* shows a typical scanned 400 keV electron image of the ice-embedded acrosomal bundle taken under flood beam illumination. It displays the characteristic (*h0l*) orientation. In the procedure used to extract the acrosomal filament, the filaments in the bundle have to be sufficiently straight along the bundle axis. Therefore, we were careful to choose image segments which are not apparently twisted for this analysis. The quantitative indication of the lack of twist is based on the small phase residual deviation from 2_1 symmetry in the phases for the computed Fourier transform of the chosen segment. Two of the three images used for single acrosomal filament isolation have defocus values of 1.5 and 5.5 mm, respectively, which were determined from the positions of the maxima and minima of the CTF rings in computed transforms, using an objective lens spherical aberration coefficient of 4.1 mm. As a result of the isolation and averaging procedure (Fig. 1, *a–d*), a single column of acrosomal filaments is shown in Fig. 2 *b*. The image of the isolated acrosomal filament has very little residual mass density next to it due to adjacent filaments, in contrast to filaments shown in Fig. 2 *a*.

The proof of the efficacy of our isolation procedure is the low density of the neighboring filaments after isolating and averaging more than 30,000 actin and scruin subunits from three images. There is a possibility that the computational procedure may introduce some errors in the region of interfilament contacts. Such interactions do occur for juxtaposed filaments, but not for the outside of the edge filaments. However, we found that the quality of the isolated acrosomal filament is quite high. First, the computed diffraction pattern has a characteristic intensity distribution consistent with the helical selection rule of 28 subunits in 13 turns. The angle of tilt in each isolated acrosomal filament was found to be <0.5°. The phases were found to obey the helical rules that dictate the relationships for odd and even Bessel orders during near/far side scaling. The extracted layer lines from the three isolated acrosomal filaments merged with a phase residual of 30° or less to 13 Å resolution, which is comparable with their crystallographic merging residuals. A threshold based on amplitude was applied, but all data above this threshold were treated equally in the phase residual calculation, without amplitude weighting.

The validity of the acrosomal filament isolation procedure is finally confirmed by the reconstruction itself, which has virtually no density that would be due to the neighboring filament columns. This in turn supports the assumption that the edge filament columns are indeed a good model for any of the internal filament columns once their lower contrast is taken into account.

Three-dimensional Structural Features of the Acrosomal Filament

Our current three-dimensional helical reconstruction has been restricted to 13 Å to simplify the analysis without the need of deconvoluting the overlap in Bessel functions in some of our layer lines. A three-dimensional density distribution of the acrosomal filament is shown as a solid surface contoured at 100% of the volume of actin and scruin (Fig. 4 *a*). In this display, we show half of the helical unit cell; the other half is related by 2_1 screw symmetry along the bundle filament axis. There are 14 actin and scruin molecules represented here in various azimuthal orientations related by a rotation of 167° and axial translation of 27.2 Å. The "barbed end" of actin is toward the bottom of this figure. The actin mass is assumed to be confined to the central region of the helix, because the acrosomal filament is F-actin based (Tilney et al., 1981), and the diameter of the actin filament is known to be <95 Å (Holmes et al., 1990). Most of the actin density is hidden behind the scruin density in this display. The actin density will be discussed below in the context of the match to the actin filament model.

The most obvious and external feature of the acrosomal filament (Fig. 4 *a*) is the massive density which we interpret to be scruin, wrapping around the outside of the filament. The mass of the scruin is divided into an elongated domain (Fig. 4 *a*, *E*) whose long axis is almost perpendicular to the filament axis, and a spheroidal domain (Fig. 4 *a*, *S*) connected to the large domain by a neck. The axis of the elon-

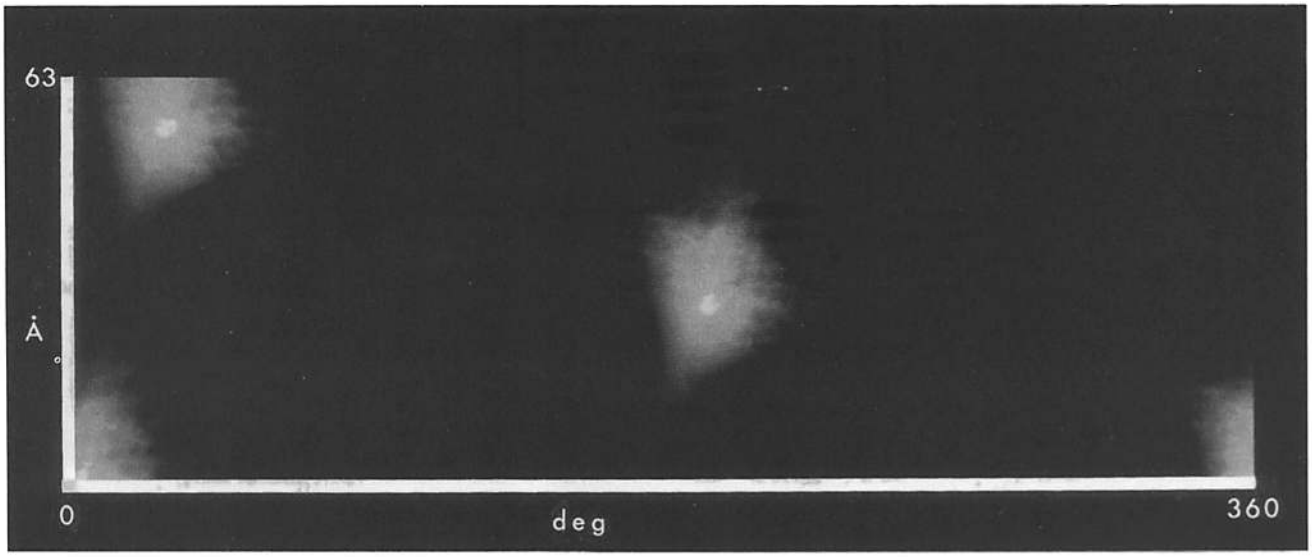

Figure 3. Display of the real-space correlation between Holmes model and our map as a function of azimuthal rotation (horizontal axis) and axial translation (vertical axis) of the model in our map. The relative magnitude of the correlation function is expressed in a gray scale with the lightest shade of gray representing the highest peaks, i.e., the best correlation between the map and the model. There is more than one peak position because the proteins repeat at an interval corresponding to the actin helical repeat (−167° of rotation and 27.2 Å of helix axis translation), but for each actin (asymmetric unit), there is only one peak position of best fit between the model and our map.

gated domain and the neck connecting to the spheroidal domain make an "elbow angle" (Fig. 4 *a*, *arrow*), which is estimated visually to be ~145°. The elongated domain lies at a lower radius than the spheroidal domain and makes more extensive contact with the actin (see below). There is little contact of the elongated domain with other scruin density along the helix, but the spheroidal domain does connect with an equivalent domain along the two-start helix by a narrow bridge.

The unit cell dimensions of a crystalline bundle and the radial extent of our density map suggests that the interactions of an acrosomal filament with neighboring acrosomal filaments are all via the scruin molecules themselves, and there is no interaction with the actin subunits of a neighboring acrosomal filament. This is probably not an artifact of the computational isolation procedure, because we make no initial assumption about the radial extent of an acrosomal filament in our procedure.

Fitting of the F-Actin Filament Model to Our Density Map

Fig. 3 shows the results of the correlation between Holmes' filament model and our three-dimensional map. With constraints based on their model, only one peak was found per asymmetric unit of the helical filament. Without such constraints, the search wrongly put the actin subunit in the scruin's density. This result was anticipated because scruin comprises 75% of the mass of the acrosomal filament. Furthermore, the search with the opposite (wrong) polarity yielded a lower correlation peak which was smeared out, and a search with the enantiomorphic structure as a test object also gave a lower peak (results not shown). In other tests, two different choices for the radial density correction gave results that varied by <2° azimuthally and 0.5 Å along the axis. Finally, searching with all the coordinates, instead of just the α carbons, gave essentially the same position for the best orientation.

Fig. 4 *b* shows the space filling F-actin filament model by itself in the orientation determined to fit best to the density map shown in Fig. 4 *a*. The actin subunits are rendered in alternating red, white, and blue. This was generated by using a radius of 10 Å for each α carbon atom in the actin structure resulting in a map of low resolution compared with the original model (Holmes et al., 1990). The x-ray structure of actin (Kabsch et al., 1990) shows four subdomains which are labeled 1, 2 , 3, and 4 in one of the actin monomers in Fig. 4 *b* as well as in the ribbon diagram of the corresponding monomer in Fig. 4 *d*. The four subdomains of an actin monomer are more obvious in certain orientations than in others along the helical F-actin filament.

Fig. 4 *c* shows our map rendered semi-transparent in green along with the actin filament in the orientation described above. 100% volume contouring levels for both our map and the actin model were used. Using the mixing of the green color representing our acrosomal filament density with the red, white, and blue colors of the actin monomers, one can visually evaluate the extent of the match between our map and Holmes' model. We observe that the model density generally matches well with the map density for actin. Some surface density of subdomain 1 in the model extends outside the boundaries of our map. Subdomain 2 is fully accounted for by the density in our map. Subdomain 3 is also fully within the density of our map and lies beneath the scruin density. In contrast to the other subdomains, subdomain 4 matches poorly to our map and has the most volume outside of our map density. Part of subdomain 2 of actin is thought to be in a different orientation in the F-actin structure (Holmes et al., 1990; Orlova et al., 1993). In our map, the match of subdomain 2 in the orientation seen in the x-ray structure is not as problematic for us as that of subdomain 4.

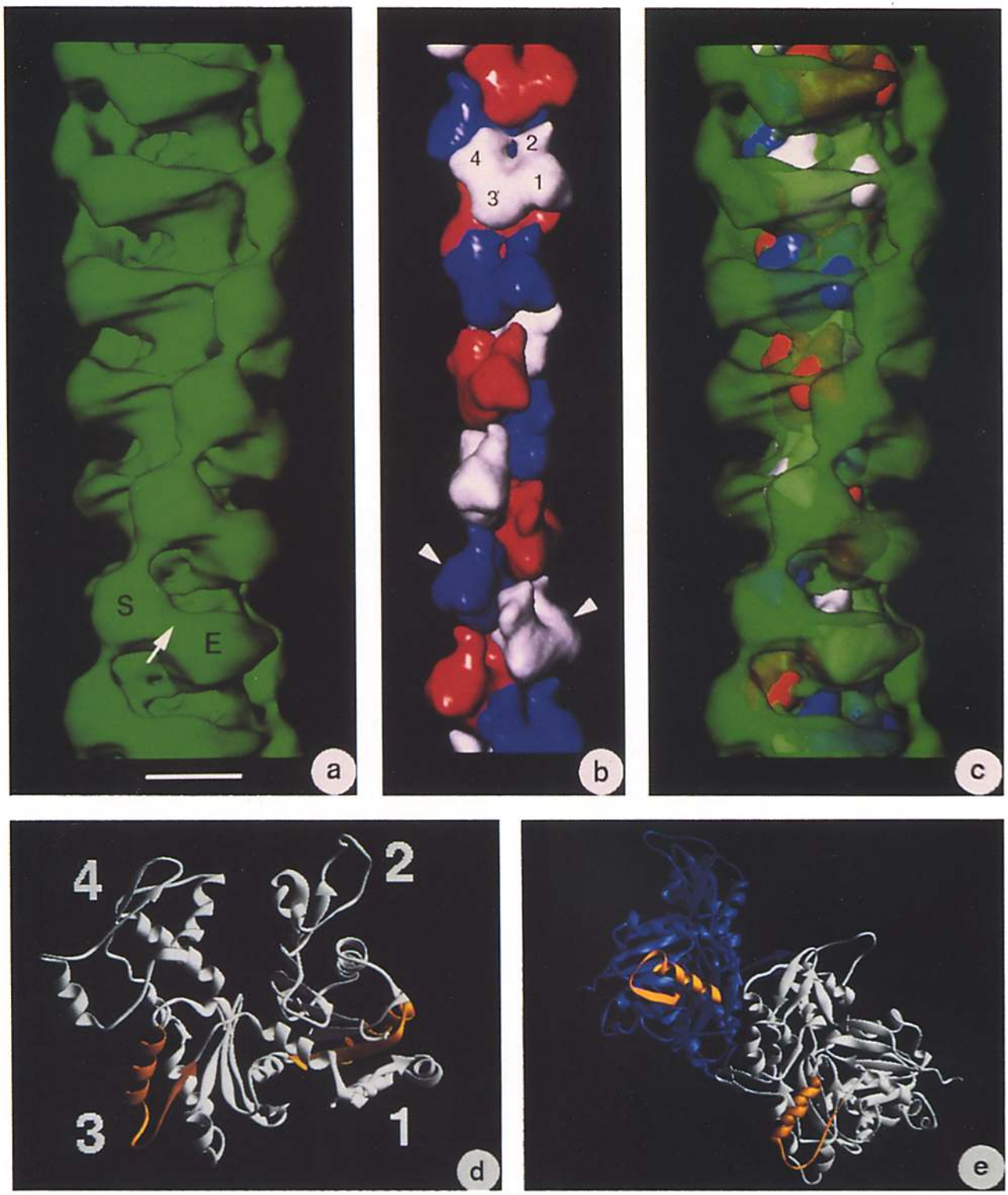

Figure 4. (*a*) The three-dimensional density map showing the overall distribution of the density of 14 scruin and actin molecules as an opaque surface rendering for 1/2 helical unit cell of one acrosomal filament (381 Å). The two domains (*S* and *E*) are labeled in one of the scruin molecules. The "elbow angle" (marked by *arrow*) between these domains is estimated visually to be ~145°. Because of the helical nature of the filament, one can visualize these two domains and elbow angle at different angular views along the filament. The scale bar represents 50 Å. (*b*) F-actin filament model of Holmes shown in the same orientation as determined in our correlation search with respect to our density map. The actin monomer is represented in three colors to distinguish the consecutive subunits more easily. The four subdomains in one of the actin monomers are labeled as *1*, *2*, *3*, and *4* according to Holmes' nomenclature. The arrows indicate the orientations of two actin subunits examined in greater detail in Fig. 4 *e*. (*c*) The superposition of the F-actin filament model of Holmes (*red*, *white*, *and blue*) in our three-dimensional density map (*semi-transparent green*). The mixed colors (such as *yellow* resulting from mixing *green* and *red*) represent regions where our map encloses or overlays the Holmes model. The green alone denotes regions of our map corresponding to scuin and/or actin in the acrosomal filament that does not match with the Holmes' model. Pure red, white, and blue denote regions

Fig. 5 shows the part of our reconstruction which occupies the same volume as Holmes' model of F-actin. The masking volume used for the model is 100% of volume expected for actin, and this cut-out map is still contoured at the same level as in Fig. 4, *a* and *c*. It illustrates that subdomains 1, 2, and 3 of actin (as were indicated in Fig. 4 *b*) match extremely well with the density in our map, and that part of subdomain 4 (the part that extends out of the density in Fig. 4 *c*) lacks corresponding density in our map. The original outline of subdomain 4 as shown in the space filling model of Holmes (Fig. 4 *b*) is indicated by a dotted line in Fig. 5 *b* for comparison. We cannot determine whether the density for subdomain 4 is disordered and therefore we cannot see it or whether the density is shifted out of the masking volume due to conformational difference of the actin in this bundle assembly from that of the Holmes' model.

Scruin-Actin Binding Sites

Our map implicates actin subdomains 1 and 3 as scruin binding sites (Fig. 4 *c*). Subdomain 3 appears to sit directly underneath the elongated domain of scruin. Fig. 4 *d* shows a ribbon diagram of an actin monomer in the same orientation as the subunit colored in white near the top in Fig. 4 *b*. Using the computer graphics display of Fig. 4, *c–e* at various orientations, we were able to deduce extensive interactions along the outside face of this subdomain, most notably involving the helix-turn-beta motif (residues 309–330) highlighted in gold in Fig. 4 *d*. This stretch of residues constitutes most of the front surface of subdomain 3. The right end of the elongated domain of scruin extends across the face of the actin filament to the edge of subdomain 1, making a small contact in the region of helix 338–348 and the loop 21–29. The spheroidal domain is connected to the elongated domain by a short neck and extends to the left around the filament and up, where it contacts the back of subdomain 1 of the neighboring actin subunit. This region of contact involves another helix-loop-beta motif (residues 113–136) in subdomain 1 (also highlighted in gold in Fig. 4 *d*). Fig. 4 *e* shows the ribbon model of two actin subunits in an orientation like that of the subunits indicated by the small arrows in Fig. 4 *b*. The two different helix-loop-beta motifs that interact with a single scruin molecule are shown in gold on these two consecutive actin subunits. This interaction also happens to be the closest distance between these sites on different actin subunits. It now becomes clear how the binding to different actin subunits along the helix stabilizes and can rigidify the actin helix for its biological function of penetration. No other bundling protein has been proposed to bind to actin in this way, "bracing" together the two strands of actin by strengthening the interaction along the one start helix. These interactions fix the relative positions of actin subunits in the filament and help fix the orientation of filaments in the bundle.

This finding is extremely interesting because subdomains 1 and 3 of the actin subunit are structurally homologous. Actin appears to have undergone a tandem duplication during evolution and both of the helix-loop-beta strand motifs lie in identical positions within these homologous subdomains (Kabsch et al., 1990). Even more interesting, we noticed that the angle between the helix-loop-beta motifs in subdomain 3 and subdomain 1 of adjacent actin subunits is complementary to the "elbow angle" that the two domains of scruin make with each other. Thus the two domains of scruin can approach the two binding motifs with the same relative orientation. The precise use of the internal structural homology within actin could be significant because the scruin also displays a tandem duplication of sequence (Way, M., and P. Matsudaira, manuscript submitted for publication). It would make sense for homologous binding domains of scruin to bind to homologous regions of the actin, because from the symmetry of the bundle these domains cannot bind to identical regions of different actin subunits.

Conserved Residues in the Helix-Loop-Beta

Though the sequence of actin from *Limulus* sperm is not entirely known, it is expected that it is similar among actins from different sources. We have used the sequence of the actin whose x-ray structure is known (Kabsch et al., 1990). Fig. 6 shows an alignment of residues in the helix-loop-beta motif of subdomains 1 and 3 based entirely on structural matching, primarily on the helix and the loop. After this structural alignment, we can determine whether there are any common features in the two sequences in equivalent three-dimensional positions. The main structural units of the motif are indicated as helix, loop, and beta. The residues with black blocks under them indicate the hydrophobic anchor residues which point to the interior of actin and do not presumably interact with scruin. The residues with a line over them are all pointed outward, and thus have the possibility of interacting with scruin. Residues that are boxed in shade are conservative for hydrophilicity or are identities in the two subdomains. Particularly striking is the *glu-lys-met* sequence in the middle of the helix from subdomain 1, which is *asp-arg-met* in subdomain 3. This could indicate the importance of charge interactions with the scruin in this region of the interaction surface. Further on, after the second *met*, there is a *phe* (*) whose corresponding structural homologue is *thr*. Normally, this would not be considered to be a conservative replacement. Inspection of the structure, however, reveals that the γ carbon (not the oxygen) of *thr* is pointed outward in the structure of actin here in subdomain 3, giving a hydrophobic patch that also occurs with *phe* in subdomain 1. This illustrates one of the dangers of using strict sequence alignment of proteins without the knowledge of the structure in assigning potential functional roles. We also lack high resolution structural information for one of the components

of the Holmes model which conversely do not match our acrosomal filament. The scale is the same as for Fig. 4 *a*. (*d*) Ribbon diagram of the actin monomer in the same orientation as that labeled with the subdomain numbers in Fig. 4 *b*. The helix-loop-beta motif in subdomain 1 (residues 107–137) and subdomain 3 (residues 304–335) are colored gold. The numbers here indicate the four subdomains. (*e*) Two actin subunits seen approximately as in the lower two indicated with arrows on Fig. 4 *b*. It clearly shows the spatial relationship between the helix-loop-beta motifs to which a single scruin binds. The motifs appear in gold in subdomains 3 and 1 of two consecutive actin subunits along the genetic helix.

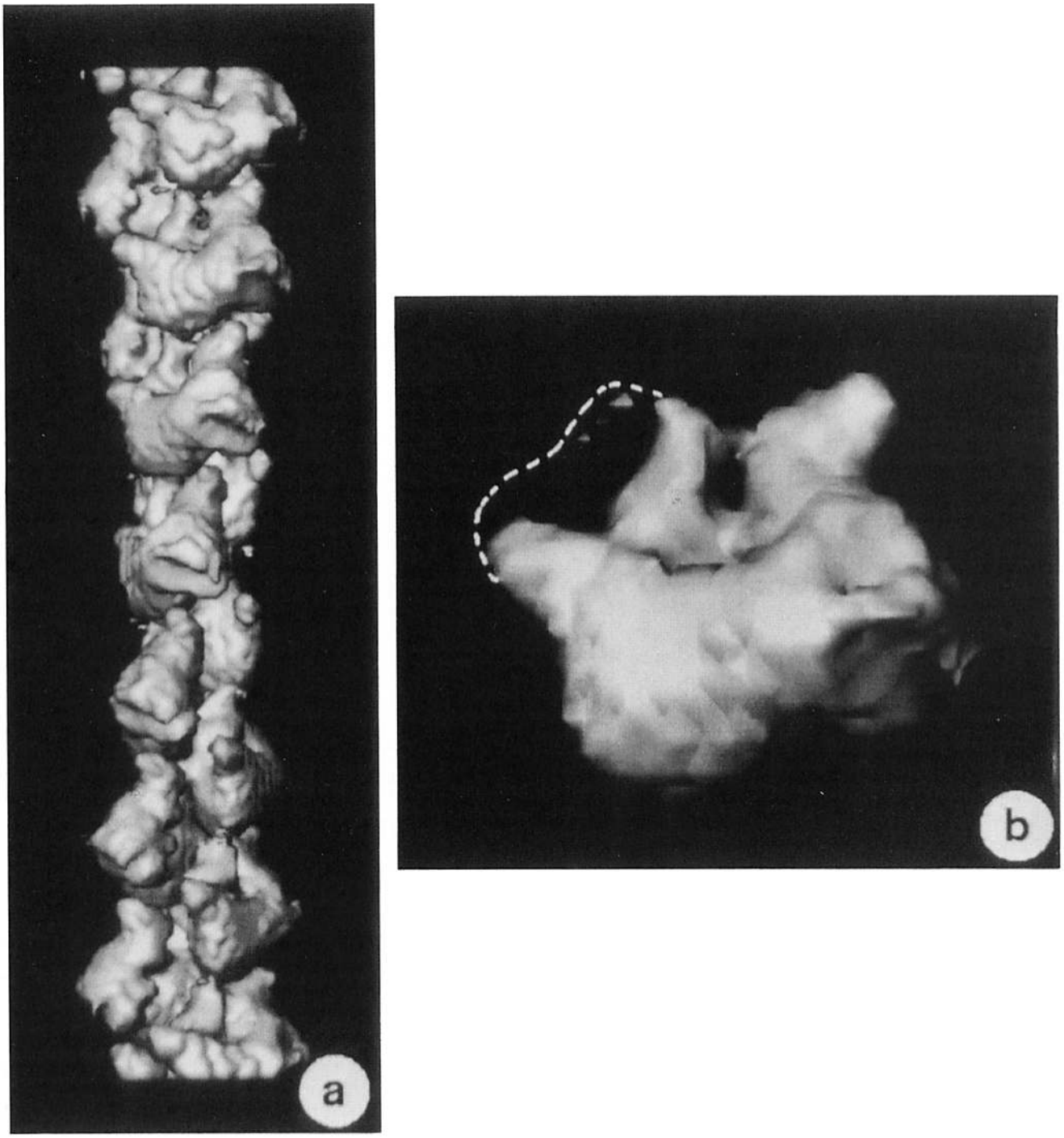

Figure 5. (*a*) The actin part of our reconstruction from the whole map which is masked out with the surface of Holmes' model in 100% volume. The volume within this surface was left with its original density, and the outside was given a density lower than the 100% volume cutoff of the map. When contoured again as shown in this figure, the part of our map outside the envelope is thus not visualized. The cut surface has a rough texture due to the masking operation. (*b*) An isolated actin molecule with the original density inside. A dotted line approximates the original outline of the Holmes' model in subdomain 4 which does not match in our density map.

of this system, the scruin. We cannot be more specific about the interactions than to indicate the general surface contact regions.

Comparison with Previous Reconstruction of Negative-stained Acrosomal Filament

Our reconstruction shows scruin is divided into two domains. In a previous study of biochemically isolated filaments from the bundle of false discharge acrosomes, Bullitt et al. (1988) presented reconstructions of the negatively stained filament decorated with 50- and 60-kD proteins, a filament decorated with the 60-kD protein alone, and a computationally generated actin filament. Our biochemical studies show the 50- and 60-kD proteins are proteolytically

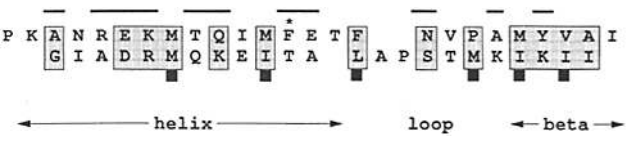

Figure 6. Alignment of the residues 112–136 in subdomain 1 (*top*) and residues 308–330 in subdomain 3 (*bottom*) of actin based on the x-ray structure. Both stretches have the structurally homologous helix-loop-beta motif. Residues with lines over them have surface side chains potentially involving interactions with the scruin; those with black blocks beneath are hydrophobic anchor residues pointing to the inside of actin; and shaded residues are conservative for hydrophilicity or identity.

derived products of scruin (Sanders, M., C. Garcia, and P. Matsudaira, manuscript in preparation) which represent the NH_2- and COOH-terminal halves of the scruin protein. Thus, comparisons between our reconstruction and their reconstruction reveals important information about the orientation and organization of domains of scruin. Their structure must be inverted to align the "barbed" end of their filament with our filament and the actin filament model. There are differences between our reconstructions in positions for scruin and actin subdomains. Their assignment of inner and outer pairs of actin subdomains is at variance with the model later proposed by Holmes et al. (1990) after the x-ray structure was known. It appears that in the en face view of the monomer, subdomains 1 and 2 are to the left in Bullitt's assignment; they are to the right in Holmes' model. Given this change, our maps of actin are similar, except theirs lacks density in subdomain 2, ours lacks density in subdomain 4. In the scruin density, their large (60 kD) domain is at low radius and situated to the side of actin subdomain 3. Our comparable region (the elongated domain) is directly over subdomain 3, and the neck we observe which connects to the spheroidal domain is in the same position as the large domain of their lower resolution map. Consequently, the rest of the outer domain (50 kD) in their map is displaced further around the filament than our outer domain, which binds to subdomain 1 as described above. Both maps would suggest that the NH_2-terminal 50-kD domain binds actin subdomain 1 while the COOH-terminal 60-kD domain binds actin subdomain 3.

Diversity in Actin Binding to Actin-associated Proteins

The polymeric nature of actin filaments permits a variety of actin binding mechanisms to exist. Some mechanisms involve binding to multiple, identical sites along a filament. For instance, tropomyosin, an elongated molecule having six or seven actin binding sites, binds along the flat face of the actin filament (Holmes et al., 1990; Milligan et al., 1990). In its "on" state, tropomyosin binds directly to the helix-loop-beta motif of actin subdomain 3. Because this site is repeated along the length of a filament, a single tropomyosin molecule can bind multiple actin subunits. It is interesting to note that tropomyosin does not appear to bind to the other homologous helix-loop-strand motif along subdomain 1 in an actin filament, possibly because the COOH-terminal portion of the monomer is in the way for the tropomyosin mode of binding. In contrast, myosin S1 binds two actin subunits in a filament. The major binding site lies on the outside of actin subdomain 1, in a region which overlaps the tropomyosin "off" binding site. A minor myosin binding site lies on subdomain 2 of the actin subunit below (Milligan et al., 1990). Despite their location on separate actin subunits, the repetitive organization of actin provides that both myosin binding sites lie in close proximity along the outside surface of the actin filament. Other proteins bind only one actin subunit. DNase I belongs to a class of proteins which bind actin monomers but not polymers. It binds to the top surface of actin subdomain 2, a region normally lying at the interface between actin subunits in a filament. When complexed with actin at this site, DNase I would sterically prevent actin polymerization (Kabsch et al., 1990).

Scruin shares a binding site (subdomain 3) with tropomyosin. This suggests that tropomyosin could compete for actin in other cells with proteins which are homologs of scruin. Scruin's contact with actin subdomain 1 is unique and this region of subdomain 1 has not been described as a binding site for any other binding protein. However, because scruin can interact with this site, other proteins may be able to bind at the same site. While bound to this site on subdomain 1, scruin would also appear to be able to sterically block myosin's nearby binding site. This conclusion is supported by the finding of Tilney et al. (1981) who have described the inability of myosin to decorate filaments in the acrosomal bundle.

Conclusions

We have developed and demonstrated a technique for isolating single acrosomal filaments from a bounded crystal of the acrosomal bundle by Fourier space phase shift and least squares minimization of the residual neighbor intensity. The lack of extra density outside the isolated acrosomal filament suggests that the procedure is successful. The atomic model of the actin filament was fit into the three-dimensional reconstruction density map and homologous loops from two domains have been implicated in the interaction with the scruin, which also happens to have homologous internal repeats. This structural homology carries over into a conserved pattern of hydrophilicity in some surface residues of the equivalent helix-loop-beta motifs in subdomains 1 and 3. This represents the first structurally equivalent use of actin's two homologous subdomains to attain an unusually tight interaction which may be essential for the stability of the acrosomal bundle.

In our approach, we have made an assumption of the presence of helical symmetry in the bundle filament. This has simplified the method of three-dimensional analysis of this complex macromolecular assembly. It is well recognized that this assumption may not be valid at higher resolution. Another potential drawback of the current approach is the lack of structural information to define molecular interactions between filaments. We will approach these questions directly by reconstruction of the entire acrosomal bundle from tilted series of images of the acrosomal bundles (Schmid et al., 1992) without any assumption of helical symmetry. Furthermore, we may be able to use more sophisticated computational approaches to retrieve higher resolution features (Schmid et al., 1993*b*) such as the secondary structure of the molecules at 7 Å or beyond.

We thank Professor Ken Holmes for providing the F-actin filament coor-

dinates and Drs. Joseph Bryan, Thomas D. Pollard, B. V. V. Prasad, and Michael Way for helpful comments on this manuscript.

This work was supported by the W. M. Keck Foundation and National Institutes of Health grants RR02250 and DK35306.

Received for publication 20 May 1993 and in revised form 13 October 1993.

References

Brink, J., and W. Chiu. 1991. Contrast analysis of cryo-images of *n*-paraffin recorded at 400kV out to 2.1 Å resolution. *J. Microsc. (Oxf.).* 161:279–295.

Brink, J., W. Chiu, and M. Dougherty. 1992. Computer-controlled spot-scan imaging of crotoxin complex crystals with 400 keV electrons at near atomic resolution. *Ultramicroscopy.* 46:229–240.

Bryan, J., R. Edwards, P. Matsudaira, J. Otto, and J. Wulfkuhle. 1993. Fascin, an echinoid actin-bundling protein, is a homolog of the *Drosophilia singed* gene product. *Proc. Natl. Acad. Sci. USA.* 90:9115–9119.

Bullitt, E. S. A., D. J. DeRosier, L. M. Coluccio, and L. G. Tilney. 1988. Three-dimensional reconstruction of an actin bundle. *J. Cell Biol.* 107: 597–611.

Carson, M. 1987. Ribbon models of macromolecules. *J. Mol. Graphics.* 5:103–106.

Chang-Yeh, A., D. E. Mold, and R. C. C. Huang. 1991. Identification of a novel murine IAP-promoted placenta expressed gene. *Nucleic Acids Res.* 19:3667–3672.

DeRosier, D. J., and A. Klug. 1968. Reconstruction of three-dimensional structures from electron micrographs. *Nature (Lond.).* 217:130–134.

DeRosier, D., E. Mandelkow, A. Silliman, L. Tilney, and R. Kane. 1977. Structure of actin-containing filaments from two types of non-muscle cells. *J. Mol. Biol.* 113:679–695.

Dolittle, R. 1992. Reconstructing history with amino acid sequences. *Protein Science* 1:191–200.

Hartwig, J. H., and D. J. Kwiatkowski. 1991. Actin binding proteins. *Curr. Opin. Cell Biol.* 3:87–97.

Holmes, K. C., D. Popp, W. Gebhard, and W. Kabsch. 1990. Atomic model of the actin filament. *Nature (Lond.).* 347:44–49.

Jeng, T. W., R. A. Crowther, G. Stubbs, and W. Chiu. 1989. Visualization of α-helices in tobacco mosaic virus by cryo-electron microscopy. *J. Mol. Biol.* 205:251–257.

Kabsch, W., H. G. Mannherz, D. Suck, E. F. Pai, and K. C. Holmes. 1990. Atomic structure of the actin:DNase I complex. *Nature (Lond.).* 347:37–44.

Kane, R. E. 1975. Preparation and purification of polymerized actin from sea urchin egg extracts. *J. Cell Biol.* 66:305–315.

Matsudaira, P. 1991. Modular organization of actin crosslinking proteins. *TIBS (Trends Biochem. Sci.).* 16:87–92.

Milligan, R. A., M. Whittaker, and D. Safer. 1990. Molecular structure of F-actin and location of surface binding sites. *Nature (Lond.).* 348:217–221.

Moore, P. B., H. E. Huxley, and D. J. DeRosier. 1970. Three-dimensional reconstruction of F-actin, thin filaments and decorated thin filaments. *J. Mol. Biol.* 50:279–295.

Rana, A. P., P. Ruff, G. J. Maalouf, D. W. Speicher, and A. H. Chishtis. 1993. Cloning of human erythroid dematin reveals a novel member of the villin family. *Proc. Natl. Acad. Sci. USA.* In press.

Schmid, M. F., P. Matsudaira, T. W. Jeng, J. Jakana, E. Towns-Andrews, J. Bordas, and W. Chiu. 1991. Crystallographic analysis of acrosomal bundle from *Limulus* sperm. *J. Mol. Biol.* 221:711–725.

Schmid, M. F., J. Jakana, P. Matsudaira, and W. Chiu. 1992. Effects of radiation damage with 400kV electrons on frozen, hydrated actin bundles. *J. Struct. Biol.* 108:62–68.

Schmid, M. F., R. Dargahi, and M. W. Tam. 1993*a*. SPECTRA: a system for processing electron images of crystals. *Ultramicroscopy.* 48:251–264.

Schmid, M. F., J. Jakana, P. Matsudaira, and W. Chiu. 1993*b*. Imaging frozen, hydrated acrosomal bundle from *Limulus* sperm at 7 Å resolution with a 400 kV electron cryomicroscope. *J. Mol. Biol.* 230:384–386.

Schmid, M. F., J. P. Robinson, and B. R. DasGupta. 1993*c*. Structure of botulinum toxin channels in phospholipid vesicles. *In* Botulinum, Tetanus Neurotoxins. B. R. DasGupta, editor. Plenum Press, New York. 397–399.

Tilney, L. G., E. M. Bonder, and D. J. DeRosier. 1981. Actin filaments elongate from their membrane-associated ends. *J. Cell Biol.* 90:485–494.

Xue, F., and L. Cooley. 1993. *Kelch* encodes a component of intercellular bridges in *Drosophila* egg chambers. *Cell.* 72:681–694.